# 3D Scanning Portable Backscatter Lidar Platform for Atmospheric Remote Sensing: Performance and Architecture overview

Francesc Rocadenbosch[a], Cecilia Soriano[b], Adolfo Comerón[a], J.M[a]. Baldasano[b], Alejandro Rodríguez[a], Constantino Muñoz[a], David García-Vizcaíno[a].

[a]Universitat Politècnica de Catalunya (UPC), Dep. of Signal Theory and Communications, Group of Antennas, Microwaves, Radar and Optics, C/Gran Capità sn., D4-016, 08034 Barcelona (SPAIN) *

[b]Universitat Politècnica de Catalunya (UPC), Dep. of Engineering Projects, 647 Diagonal Ave. 10th., 08028 Barcelona (SPAIN)

EUROPTO. Remote Sensing of Clouds and the Atmosphere V. SPIE Proceedings vol. 4168 (2001)

## ABSTRACT

This article is aimed at describing the technology, system architecture and specifications of a new 3-D Nd:YAG scanning lidar. Main features of the system are interspersed low-range (typ. 500 m - 4 km) and far-range exploration (typ. 4 km – 50 km), open user-configurable scanning tools and a specific architectural design based on parallel CPU control, a LabView™ user interface and a digitally controlled optoelectronic receiver. The latter provides key advantages to the whole system architecture such as calibration of lidar returns in terms of absolute power and repeatability.

Issues concerning system responsivity calibration, receiver gain self-calibration, automatic gain control and synchronization, offset-drift zeroing and the like, all of which are of prime importance for the lidarist, are presented. As far as we know, these contributions are new to the state-of-the art of the community of optical and electronic lidar system designers.

**Keywords:** lidar, backscatter lidar, remote sensing, system design, responsivity, control.

## 1. INTRODUCTION

Since as early as 1967 when Fiocco and Smullin [1] first bounced a laser beam off the moon, elastic-backscatter lidars provide a unique highly-spatially-resolutive tool for aerosol content monitoring, ceilometry studies (cloud-height extent) and environmental control [2]. Pulsed elastic lidars are remote sensing instruments that take advantage of the relatively strong interaction among the emitted laser pulses and the aerosols and molecules in the atmosphere (Mie and Rayleigh scattering). As a result, the backscattered radiation (at the same wavelength as the incident one) conveys information about the atmospheric state in terms of range-dependent extinction and backscatter profiles, from which using either co-operative instrumentation or a priori assumptions, it is possible to retrieve physical parameters of concern [3].

Since 1993, the Polytechnic University of Catalonia (UPC) has been involved in the design and construction of lidar instruments and inversion algorithms [4][5][6][7]. As regards to backscatter systems, a 0.5-J Nd:YAG pulsed backscatter lidar fixed lidar station was built in 1996 and since then, a fairly interesting 3-D 0.35-J Nd:YAG scanning portable lidar has been developed. A more stringent specification for this system was that it had to able to perform both short- and far-range (stratospheric) exploration in dual window mode. The motivation for this design specification is discussed in Sect.2 and its architectural implementation in Sect. 3. Sect. 4 outlines the main features of the digital optoelectronic receiver masterpiece, Sect. 5 presents an algorithm for absolute responsivity calibration and Sect. 6 a photographic overview of the lidar instrument.

## 2. DYNAMIC RANGE AND THE DUAL WINDOW APPROACH

Usually, common backscatter lidars have a receiver chain that comprises an optoelectronic receiver and a 10-to-12-bit acquisition card. The former basically consists of either an avalanche photodiode (APD) or a photomultiplier tube (PMT) followed by a transimpedance amplifier (i.e., a current-to-voltage converter), whereas the latter is an analog-to-digital converter (ADC) in a PC. Since each bit of the ADC equals 6 dB dynamic range in terms of voltage output (equivalently, 3 dB/bit in terms of power levels at the receiver input), a typical 12-bit card offers 72(36) dB voltage (power) dynamic range.

* Correspondence: (F.R.) E-mail: roca@tsc.upc.es; WWW: http//www-tsc.upc.es/eef; Telephone: 34-93-401-60-85; Fax: 34-93-401-72-32.

In practice, this figure is limited by inherent electronic thermal noise in the card so that a practical figure usually lies in the 60-65 dB interval. This is to say that for most systems, the maximum and minimum detectable voltage levels V(R) at the receiver output can only differ in three orders of magnitude or so. It appears that the equivalent receiver chain prior to the acquisition card performs the following linear conversion

$$V(R) = R_i G P(R) + V_{OS} \tag{1}$$

where V(R) is the analog voltage [V] at the receiver output (equivalently, at the acquisition card input), P(R) is the input lidar backscattered return power [W], $R_i$ is the detector current responsivity [A/W] (a function of the polarization voltage), G is the equivalent variable transimpendance gain [V/A=Ω] of the receiver chain, where $G \in [G_{min}, G_{max}]$ and $V_{OS}$ [V] is the net equivalent offset at the receiver output. In fact, $V_{OS}$ merges into a single body background-power induced (e.g. solar background), unwanted electronic biases plus a digital-to-analog (DAC) user-generated bias used as offset correction.

Eq.(1) states that one can see the optoelectronic receiver as a linear transformation that maps P(R) into the $\pm V_{max}$ limit of the bipolar acquisition card using the most appropriate settings of receiver gain, G, and net offset, $V_{OS}$, , for each atmospheric scene at hand. In order to make the most from the ADC dynamic range, two system operation conditions must be met:

1) System-generated offset $V_{OS}$ must be set so that very far returns, for which $P(R \to \infty) = P_{back}$ with $P_{back}$ the background component, are mapped to $V(R \to \infty) = -V_{max}$. Using Eq.(1),

$$V_{OS} = -V_{max} - R_i G P_{back} \tag{2}$$

2) Gain G must guarantee that peak returns along the exploring range do not saturate the digitizer. Very often, return power peaks occur at the range of full overlap between the laser beam and the telescope field-of-view, $R_{ovf}$, or in cloud regions. If $P_{max}$ denotes the maximum return intensity of these peaks, the gain setting becomes

$$G = \frac{V_{max} - V_{OS}}{R_i P_{max}} \tag{3}$$

Given conditions (1) and (2) above, Eqs.(2)-(3) enable to solve the optimum settings for the two unknowns, G and $V_{OS}$, that best accommodate the mapped voltage return signal V(R) (Eq.(1)) into the dynamic range of the acquisition card. In theory, given optimum settings for G and $V_{OS}$, Eq.(1) enables to fit any optical power dynamic range [$P_{max}$, $P_{back}$] into that of the acquisition card. In practice, one should replace $V_{max}$ by $V_{max}' = V_{max} - \Delta V_0$ in Eqs.(2)-(3), with $\Delta V_0$ some security threshold to avoid noise clipping and, therefore, pulse averaging distortion.

From a practical point of view, if a bipolar ADC were used, the system A-scope should draw

$$V'(R) = V(R) - V(\infty) \tag{4}$$

The procedure outlined above is illustrated in Fig.1. This real example uses a ±1-V 12-bit acquisition card (CompuScope 1012 from GaGe™ Applied Sciences) and the plots represent V'(R) from Eq.(4), so that the background power return $P_{back}$ is mapped to V'(R) ≈ 0V and the absolute maximum of the exploration range, $P_{max}$, to some tentative 2V (the ADC dynamic range) in the vertical scale. Fig. 1(a) shows a 15-km 1.5-V data record and Fig.1(b) its range-corrected representation. Alternatively to Eq.(2) the $V_{OS}$ setting has been estimated by spatial averaging samples in the 95-100-km range, where the signal is thought to be extinguished. As seen in Fig.1(a)-(d), the $V_{OS}$ setting turns out to be fairly well adjusted because the noisy signal return from 13-to-15-km range is above the baseline.

Before proceeding further, it is interesting now to define the averaged quantization error, $\varepsilon_q^M$. If ν is the number of bits of the ADC and M the number of integrated pulses, then $\varepsilon_q^M$ can readily be computed as [8]

EUROPTO. Remote Sensing of Clouds and the Atmosphere V. SPIE Proceedings vol. 4168 (2001)

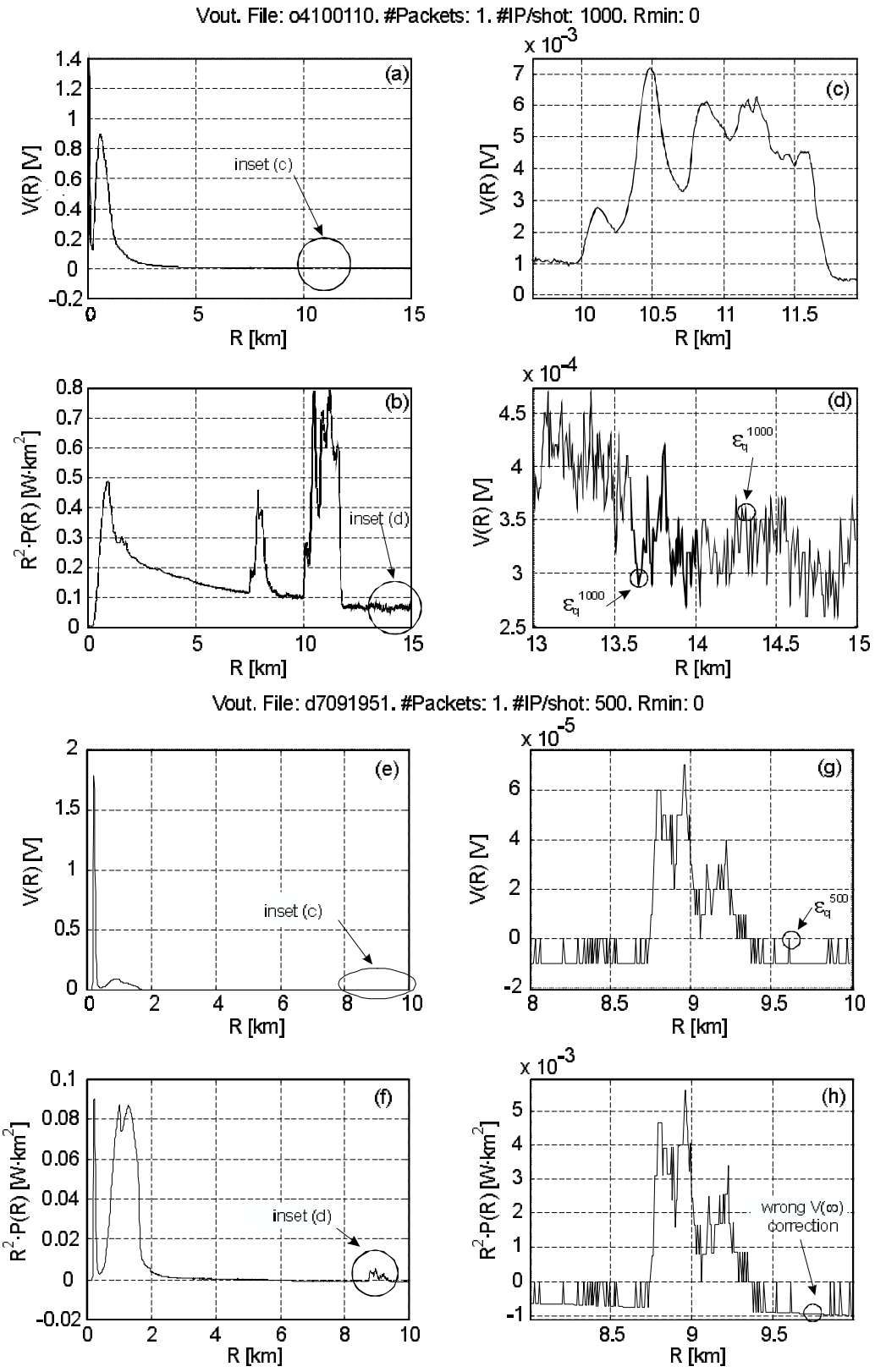


Fig.1 Single window is enough for case example I in subset (a)-(d). Double window is required for case example II in subset (e)-(h).

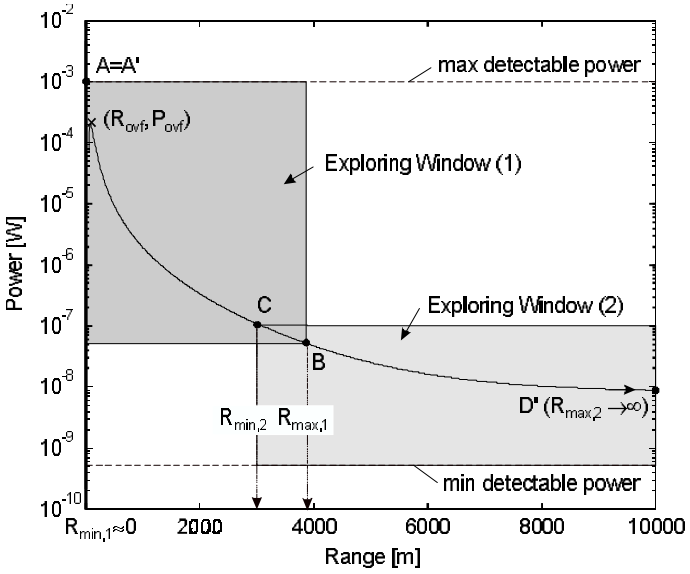


Fig.2 The double-window technique. Using double window exploration and synchronous gain and offset conditioning, the equivalent dynamic range of the lidar system can largely be expanded. Thus, instead of fitting the full lidar exploration range (A'-D') into the dynamic range of the ADC, a partitioned approach is used to accommodate range A-B into the ADC at the odd pulses and range C-D at the even ones. At each succeeding shot, the system ping-pongs gain and offset receiver settings accordingly. As a result of this dual-mode operation, the lidar is able to perform interspersed short-range [$R_{min,1}$, $R_{max,1}$] (AB window) and far-range [$R_{min.2}$, $R_{max.2}$] (CD window) exploration.

$$\varepsilon_q^M = \frac{1}{2^v\sqrt{M}} \tag{5}$$

For M=1000 integrated pulses, this yields $\varepsilon_q^{1000}$ =7.7μV, which is the approximate size of the averaged quantization noise spikes inside any of the circles in Fig.1(d). In addition, Fig.1(c) shows good quantization of the cloud layer segment lying in the 11-km range (see inset label in Fig.1(a)).

The situation is, however, quite different for the scene shown in Fig.1(e)-(h). Again, gain (G) and offset ($V_{OS}$) settings have been finely tuned to ensure best fitting of the lidar return signal into the 0-2V dynamic range of the ADC and V'(∞)=0 (see Fig.1(e)(f)) but, in spite of the actual settings, it turns out that gain G is not high enough to ensure proper recording of the weak cirrus returns in the 8-10-km range. This is because the number of ADC excited levels is only few times the averaged quantization noise $\varepsilon_q^{500}$. This phenomenon is be better evidenced in Fig.1(g), where the cirrus cloud return peak of interest is about 8 times greater than $\varepsilon_q^{500}$ ($\varepsilon_q^{500}$ =1.1×10$^{-5}$ V for M=500 pulses averaged). Bad acquisition of the return signal at the far ranges causes, in turn, wrong estimation of the V(∞) correction in Eq.(4). As a result, V'(∞) fluctuates from shot to shot around the baseline of Fig.1(h) and it yields to meaningless results once data inversion is performed. Similar situations are likely to occur if simultaneous short and far-range (stratospheric) explorations are to be fitted at once into the 12-bit ADC. This mode of operation is called single exploration window for the ADC acts as a recording window along the exploration range of interest.

There is a way out, however, if such exploration range is divided into two (or more) exploring windows that use different G and $V_{OS}$ settings for each partitioned range. The solution is illustrated in Fig.2 and explained next in Sect.3. Assuming 65-dB ADC effective dynamic range in single window operation mode, the dual window approach will grant some 130-dB equivalent ADC dynamic range.

## 3. SYNCHRONIZATION AND ARCHITECTURE OVERVIEW

Dual-window operation and 3-D scanning features make system synchronization (sync.) more involved. For this reason and to specialise hardware unit functionality, a multi-CPU approach is followed. Fig.3 depicts a hardware set-up diagrammatic, Fig.4 the synchronization chronogram among the involved signals and units and Tab.1, main system specs. Fig.4 assumes a repetition rate of 20 Hz or, equivalently, a 50-ms pulse repetition time (PRT).

The core of the sync. system consists of the control unit and a digitally controlled patented optoelectronic receiver [9] (Tab. 2). Outstanding features of this receiver are that its gain and offset can be programmed via a digital bus and that a very fast enable feature permits both precise timing of the receiver listen window, when enabled, and very large output isolation, when disabled.

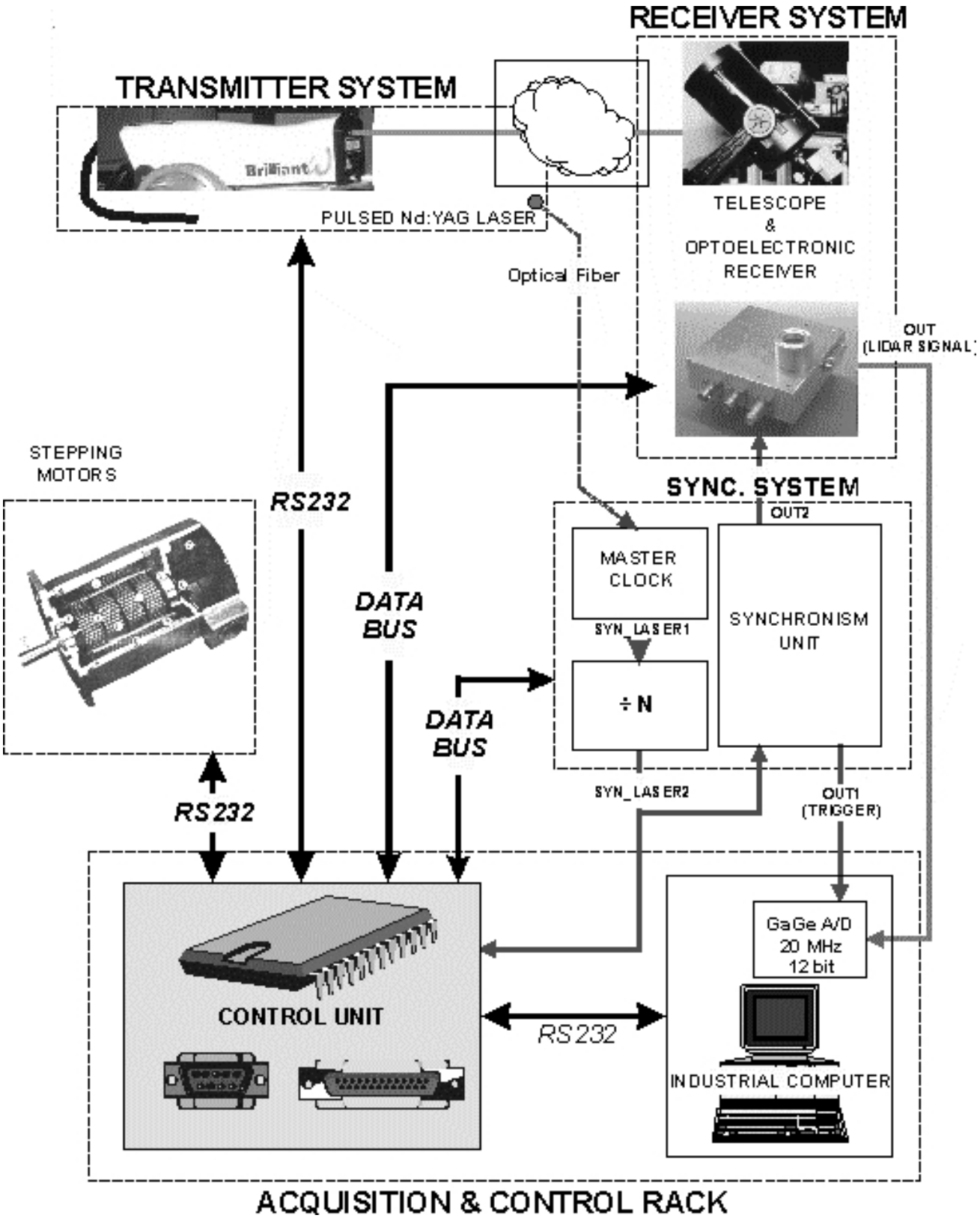


Fig. 3 Lidar system architecture overview showing main units.

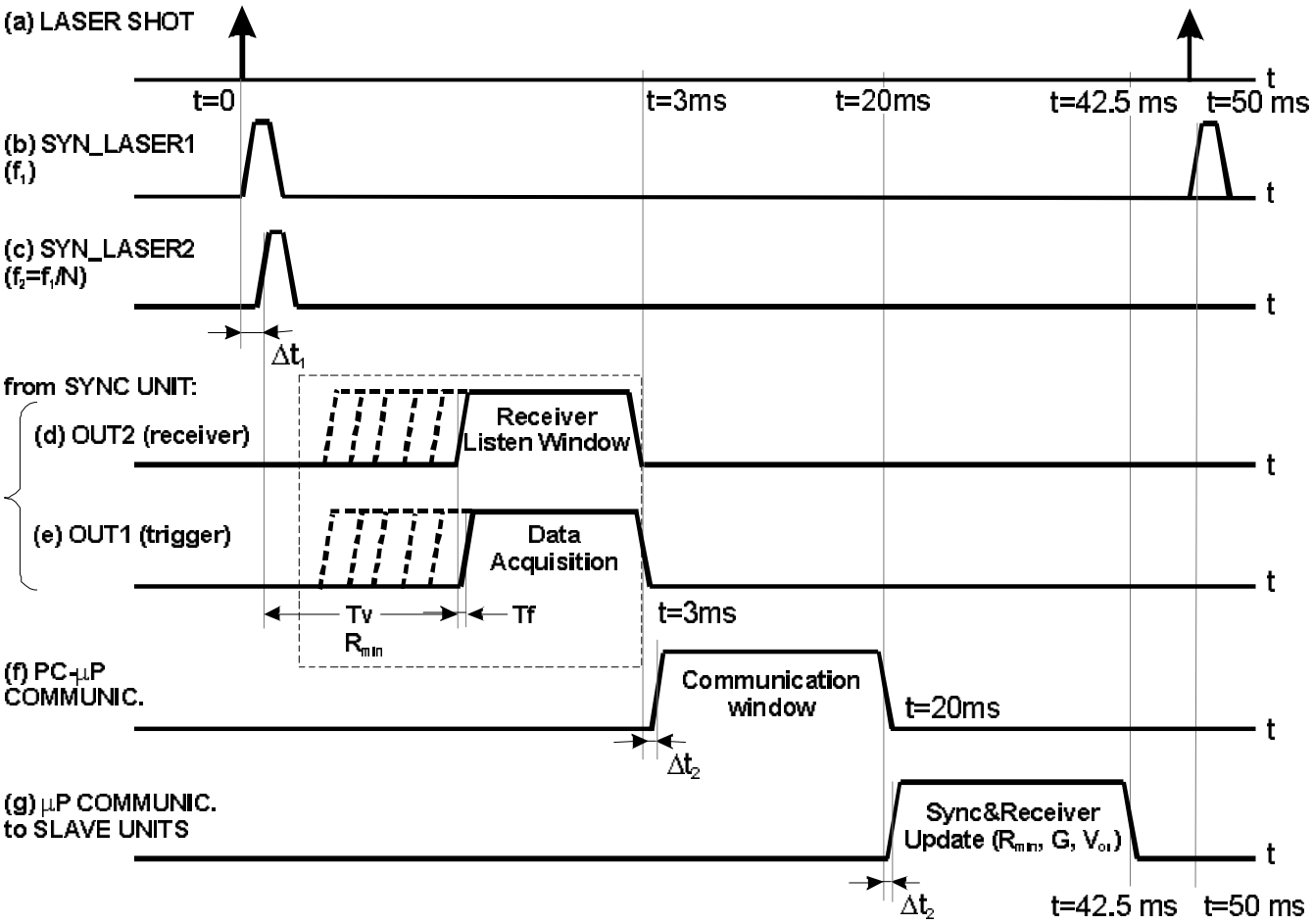


Fig. 4 Synchronization diagram. (a) Laser shot period (rep. rate = 20 Hz). (b) Sync. signal at the master clock output. (c) Sync. signal at the frequency prescaler output (for test purposes). (d) Optoelectronic receiver enable window. Its variable time length sets the lidar receiver range. (e) Trigger signal to the acquisition card. (d) and (e) signals are both issued from the synchronization unit. Precise timing of (d) and (e) signals is necessary to ensure accurate interspersed short-range and far-range exploration. (f) At each pulse repetition period (PRT=1/$f_1$) a 17-ms time frame ([3-20] ms) is reserved for data communication between the LabView application on the computer side and the μP control unit. Whenever necessary, the computer passes new position parameters for the stepping motors and gain, offset and timings data sets for the exploring windows on to the control unit. (g) At each PFT, the control unit uses a [20-42.5] ms time frame to issue refresh data signals to its slave units (receiver and sync. unit).

The receiver has memory buffers so that it can operate using some predetermined gain and offset settings ($G_1$, $V_{OS,1}$) while the required ones for the next laser shot ($G_2$, $V_{OS,2}$) are be stored in its back-up memory. Settings update can either be synchronous to an external signal or asynchronous, though for the present application they are obviously synchronous.

System operation assumes a prior training stage where the user edits the lidar scan trajectory and defines some initial pairs ($G_1$, $V_{OS,1}$, $R_{min,1}$ ) and ($G_2$, $V_{OS,2}$, $R_{min,2}$) (see Fig. 2). During normal operation the computer monitors the recorded signal V'(R) and makes on-line corrections for the actual settings. This prevents saturation of the signal in case of visibility changes, moving clouds or thermal drifts that induce offset drifts in the receiver. Normal operation consists of a loop sequence that can be explained as follows (refer to Fig. 3 and Fig. 4):

When the laser shots ((a) in Fig. 4) a little amount of scattered light is coupled into an optical fiber located nearby the laser aperture so that the fiber transmits this light sample into the master clock unit. Upon reception of this fire sample, the master clock issues a TTL-logic SYN_LASER1 signal ((b) in Fig. 4). Here, we note that if very fine zero-range calibration is not

needed, most manufactured synchronism laser signals would serve the purpose of the master clock so that it could be made redundant. Signal (c) in Fig.4 can either be signal (b) in Fig. 4 or a frequency divided version of it, which is often used for test purposes. Thus, identifying SYN_LASER2 signal with SYNLASER1, SYN_LASER2 is used to inform the sync. and control units that a laser pulsed has been fired. At this time, the sync. unit starts different time counts. Time-out occurs when the programmed time $2R_{min,1}/c$ (for the "exploring window 1" in Fig.2) or $2R_{min,2}/c$ (exploring window 2) is reached. In practice, these times take into account intrinsic transmission line delays. Likewise, at time-out the sync. unit emits two signals slightly delayed to one another in order to enable the receiver listen window ((d) in Fig.4) on ahead and to trigger data acquisition ((e) in Fig.4). Lidar signal acquisition comprises the required number of samples according to the temporal (spatial) length of the current exploring window (for instance, assume range A-B in Fig. 2) plus a few ones around t=3ms. The latter ones are averaged to estimate $V(\infty)$ in Eq.(4) (note that t=3ms equals 450 km!, therefore, this time can be assimilated to $R \rightarrow \infty$). Once the acquisition has been finished, handshake signals can be established between the computer and the control unit during a 17-ms time frame ((f) in Fig.4). Offset thermal drifts or sudden changes in the atmospheric scenario may trigger correction orders from the computed side. If changes are needed, the computer sends a data burst consisting of the actual absolute coordinates for the azimuth and elevation steeping motors plus two sets of four parameters formatted as ($t_v$. $t_f$, G, $V_{OS}$). Each of these sets fully defines an exploring window in terms of the required gain, offset, receiver enable time $t_v$ and, relative ADC trigger delay $t_f$; the latter two parameters determining the minimum exploring range settings for the actual exploring window ((d), (e) and (g) in Fig. 4). Upon reception, the control unit decodes and splits this information into appropriate data protocols for its slave units. Thus, a routing head is added to the coordinate position data fields for the stepping stepping motors, and the ($t_v$. $t_f$, G, $V_{OS}$) data set is passed on to the receiver and sync. units according to their own data protocols and communication timings. By t=42.5 ms the control unit issues a refresh signal to the receiver so that the new G and $V_{OS}$ settings for the next laser shot are updated and latched. If the computer does not request changes in the exploring window parameters (i.e., if no PC-μP communication is received from line (f), Fig.4), then the two exploring window sets, ($G_1$, $V_{OS,1}$, $t_{v,1}$, $t_{f,1}$) and ($G_2$, $V_{OS,2}$, $t_{v,2}$, $t_{f,2}$), will continue to be send to the receiver and sync. units at each succeeding fire in ping-pong mode. Besides this basic routine, the control unit oversees its slave units. Thus, for instance, the control unit performs an initial test during the start-up sequence, it monitors alarm position switches and it bypasses start/stop and energy orders from the computer to the laser.

In summary, the dual window approach emerges as an efficient synchronous mechanism for automatic gain control, dynamic range enhancement and offset-drift zeroing.

## 4. RECEIVER FEATURES

Even for single-window operation, lidar receivers should at least exhibit four main characteristics:

*1) Low-noise.* For an APD-based receiver, as is the case, there are two main limiting situations in terms of signal-to-noise ratio (S/N): the first regime or *signal shot-noise limited mode* occurs when noise due to the primary photocurrent (i.e., the lidar return power induced current on the APD) becomes dominant. Following [4][10] the S/N ratio can be expressed as

$$\frac{S}{N} = \left( \frac{R_{io} L}{2 q B_N F(M)} \right)^{\frac{1}{2}} P(R)^{\frac{1}{2}} \tag{6}$$

where $R_{io}$ is the APD current responsivity without gain multiplication (i.e., for M=1) [A/W], L is the optical loss term [dimentionless], M is the APD gain [dimentionless], F is the excesss noise factor [dimentionless], which is a function of the gain M, $B_N$ is the noise equivalent bandwidth [Hz], P(R) is the return power [W] and, q is the electron charge [C].

Eq.(6) underlines that for short ranges, which may well be the case of the "exploring window 1" in Fig.2, a low F is needed, equivalently, a low NEP photodiode [10]. Note that this conclusion does not depend on the receiver gain G, which acts as a signal conditioning parameter (Eq.(3)).

2) *Large gain.* Continuing with our previous discussion, the second regime or thermal-noise limited mode, the reader is more familiar with, yields that

$$\frac{S}{N} = \left( \frac{R_{io} MGL}{\sigma_{th} \sqrt{B_N}} \right) P(R) \tag{7}$$

where G is the equivalent transimpedance gain in [V/A], $\sigma_{th}$ is the amplifier input noise current density [$A \cdot Hz^{-1/2}$] and, the rest of parameters have already been defined in Eq.(6). Note that $R_v = R_{io} MG$ equals the total receiver responsivity [V/W].

In the thermal-limited mode, which corresponds to far-range exploration ("exploring window 2" in Fig.2) the S/N degrades faster ($1/R^2$) than in the shot-limited mode (1/R). Consequently, the system benefits the most from large receiver gains G, since the larger G, the better the S/N. Large gains put however some difficulties to electronic design. Usually, several stages are needed and decoupling and dominant-pole techniques must be used to prevent oscillation. Particularly from the lidarist point of view, another important consequence is that large gains do mean large offsets at the receiver output and what is more, magnification of their thermal-drifts. In the case of our lidar receiver, remote digital offset adjustment is a must.

*3) Wide dynamic range for G.* Assuming the simplifying condition $P_{back} \approx 0$ in Eq.(2) and expressing Eq.(3) solution in log-form, the gain variability is directly related to the variability in the expected $P_{max}$ as

$$G(dB) = \log\left( \frac{2V_{max}}{R_i} \right) - P_{max}(dB) \tag{8}$$

A concluding remark from Eq.(8) above is that the dynamic range of G equals that of the peak return powers one wishes to be capable to handle. Since $P_{max}$ strongly depends on the atmospheric scene at hand and specific system geometrical settings, it is strongly advisable to have a variable gain G [V/A] (equivalently, a variable responsivity $R_v$ [V/W]) as large as possible, 30 dB being an acceptable figure for most common single-window lidar systems.

*4) Appropriate bandwidth.* This is a well-known parameter so that according to the Nyquist sampling criterion [8], $B_N$ must always be less than half your sampling rate. Yet, this requirement combined to requirement no.2 above often forces unpractical gain-bandwidth products so that several amplification stages are needed.

| RECEIVER PARAMETER | MIN | TYP | MAX | UNITS |
|---|---|---|---|---|
| **Optical Power Levels** | $10^{-10}$ | | $2 \cdot 10^{-3}$ | W |
| **Responsivity (note 1)** **($\lambda_1$=830 nm, $\lambda_2$=1064 nm)** | $1.4 \cdot 10^3$ ($\lambda_1$) $6.5 \times 10^2$ ($\lambda_2$) | | $10^8$ ($\lambda_1$) $4.7 \times 10^7$ ($\lambda_2$) | V/W |
| **Bandwidth** | DC | | 9.2 | MHz |
| **NEP (noise equivalent power)** | | 40 | | $\frac{fW}{\sqrt{Hz}}$ |
| **Offset adjustment (note 2)** | 0.04 | | 7.6 | mV/LSB |
| **Enable Time** | | 380 | | Ns |
| **Disable Time** | | 1.1 | | μs |
| **Dimensions (length×width×height)** | | 125×115×55 | | Mm |

**Notes:**
(1) Tentative specs between 100 MHz-1GHz upon request.
(2) Output offset adjustment for 1-LSB variation. MIN → at minimum conditioning gain; MAX → at maximum conditioning gain.

Tab. 1 Main specs of the digitally controlled optoelectronic receiver developed.

EUROPTO. Remote Sensing of Clouds and the Atmosphere V. SPIE Proceedings vol. 4168 (2001)

For dual window operation, the specs are still more demanding and they require a digitally controlled optoelectronic receiver with variable gain and offset adjustment and a fast enable/disable feature. In addition to these specs., the optoelectronic receiver prototype presented in Tab. 1 also includes a low-rate built-in 16-bit ADC for miscellaneous purposes. Moreover, the receiver can be coupled to many optical instruments using mechanical add-ons so that its applications are not only limited to lidar but to medium-rate non-guided communications as well. The figures shown in Tab. 1 assume a built-in C30954 APD from EG&G.

## 5. RESPONSIVITY CALIBRATION

Responsivity calibration ($R_v$ in units of [V/W]) permits to calibrate the lidar return signal in terms of absolute power [W]. This feature enables the presented lidar instrument to act as an absolute photometer. An interesting application of this is the possibility to perform solar radiance measurements for they play an important role in the earth heat exchange radiation budget.

In order to calibrate the receiver total responsivity $R_v$ ($R_v=R_iG$ in Eq.(1)), the basic set-up consists of the lidar instrument shown in Figs.5-7, a mechanical chopper and a precision low-power calibrated diode laser. Light from the diode laser is directed into the telescope via the chopper, which is used to modulate a 1-kHz signal. Since the modulated response can easily be separated from the offset component of Eq.(1) and V(R) reproduces the square wave in P(R) times the total responsivity $R_v$, $R_v$ can be estimated as $\Delta V/\Delta P$.

Since the bus-controlled architecture of Fig.3 enables automatic measurements to be performed and saved for each of the *n=64* programmable gains (G) and for each of the *m=400* APD polarization tensions (we use a Standford Research PS-350 GPIB supply in 1-V steps), calibration of $R_v$ is straighforward. The accuracy of the calibration algorithm is basically limited by the power measurement uncertainty of the calibration laser used and by thermal and quantization noises that add on the acquired samples. Fortunately however, the latter error sources can be minimized by means of averaging. Furthermore, the number of calibration measurements can be reduced from *n×m* to *n+m*, using the following two-step procedure:

a) First, for a given APD polarization, sweep all the *n* receiver programmable gains G. If we depart from Eq.(1) and we neglect the offset term $V_{OS}$ (for it has nothing to do with the square-wave signal component), the measurement vector for step 1 results in

$$V_{1j} = R_1 G_j P_{opt} \qquad j = 1..n \tag{9}$$

where $V_{ij}$ is the measured peak-to-peak voltage readout, $R_i$ the APD current responsivity for the i-th polarization voltage setting and $G_j$ is the j-th transimpedance receiver gain setting.

b) Second and last, for a given gain $G_1$, sweep all the *m* APD polarization tensions in 1-V steps. This yields

$$V_{i1} = R_i G_1 P_{opt} \qquad i = 1..m \tag{10}$$

Therefore, net responsivity $R_v(ij)$ can be computed as

$$R_V(i,j) = R_i G_j = \frac{V_{i1} V_{1j}}{V_{11} P_{opt}} \tag{11}$$

in *n+m* measurements only. Calibration algorithm efficiency is obviously lower than using n×m redundant measurements and again it can be estimated using standard error propagation techniques [11].

Though this solution is still not implemented, we are thinking of fixing a chip diode laser on/off modulated on telescope primary lens and of integrating the whole calibration procedure into the LabView control application.

EUROPTO. Remote Sensing of Clouds and the Atmosphere V. SPIE Proceedings vol. 4168 (2001)

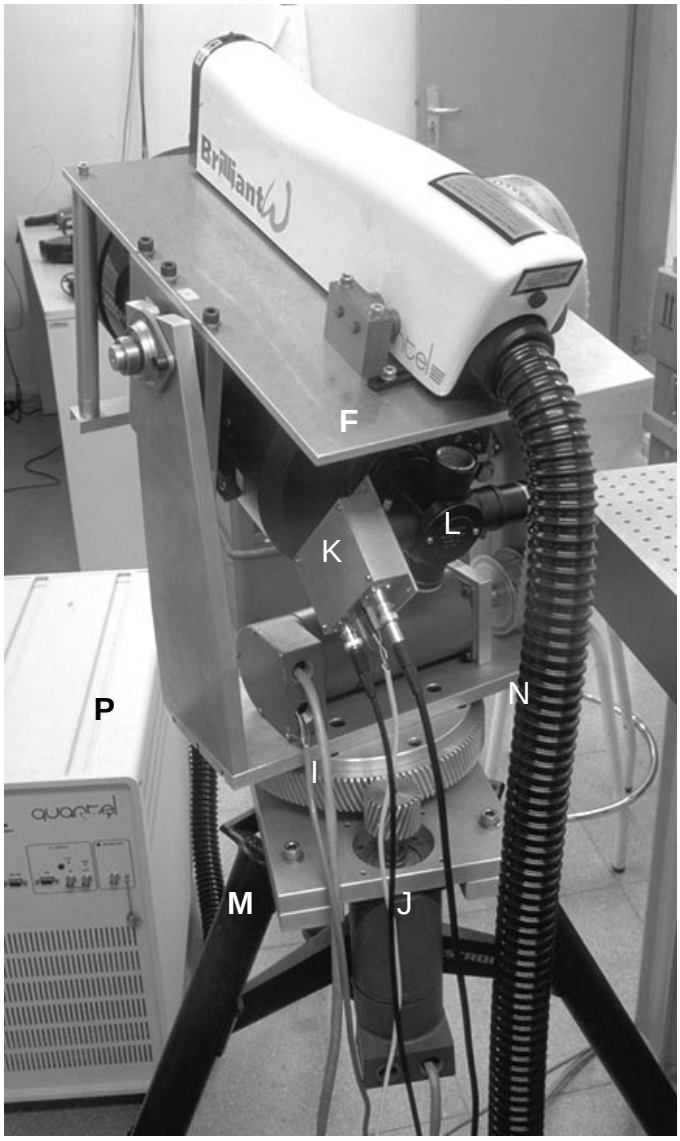


Fig. 5 (Top left) Rear view of the 3-D scanning portable lidar. You see, the laser (A) mounted on top of the aluminium platform (F), the reduction gear set (I) for the azimuth movement and its stepping motor (J) and, the digital receiver (K) coupled in place of the eye-piece. Other slots for eyepieces are coupled to the telescope by means of a rotary ball-and-socked joint (L). The whole structure is mounted on a tripod (M) so that it can rotate some 300° in azimuth, this figure limited by the strain on the laser hose (N), which is bounded to the laser power supply (P).

Fig. 7 (Bottom right) Front panel of the LabView™ control application running on the industrial computer. The control panel offers full control over all system units shown in Fig.3 as well as responsivity calibration options and a scan trajectory vector editor.

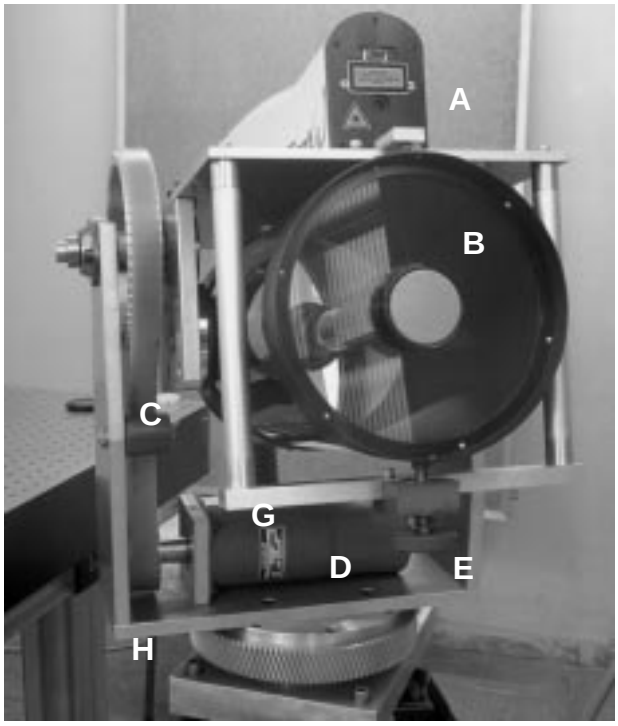


Fig. 6 (Top right) Front view of the 3D scanning portable lidar showing the laser (A), the receiving telescope (B), the elevation gears and belt (C), the stepping motor (D) and a micrometer elevation screw (E) for overlap factor adjustment. The laser platform (F) and the telescope are assembled in an aluminium frame (G), which enables the elevation movement. The whole structure is mounted on a U-fork (H), which rotates in azimuth. For transportation the U-fork can be disassembled from the tripod.

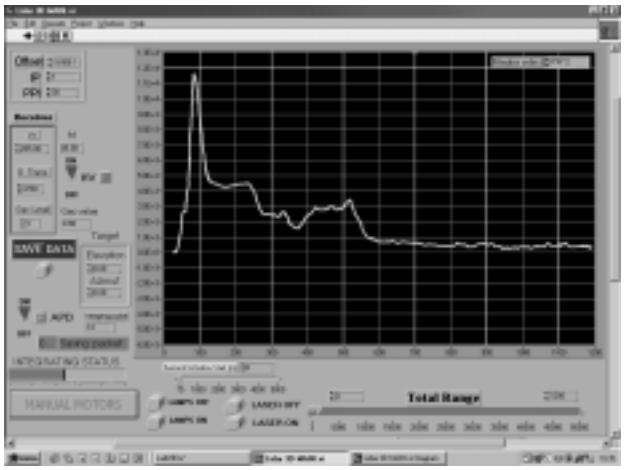

## 6. THE LIDAR SYSTEM INSTRUMENT

Presentation of the 3-D dual-window portable backscatter lidar is done in form of a photographic tour along Fig.5-Fig.7. Main systems specs are summarized in Tab. 2.

| SYSTEM SPECS | | |
|---|---|---|
| **Scanning capabilities** | **Scanning range** | 120º × 300° |
| | **Angular precision** | 30 arc sec. |
| **Transmitter** | **Laser specs** | Nd:YAG 1064 nm |
| | | 0.35 J / 0.5 mrad |
| | **Pulse specs** | 10 ns / 20 Hz |
| **Telescope** | **Diameter** | 20 cm |
| | **Focal length** | 2 m |
| **Receiver** | **Min. Det. Power** | < 0.5 Nw |
| | **Acquisition** | 20 Msps/12 bit |
| | **Spatial resolution** | 7.5 m |
| | **FOV** | 1.5 mrad |

Tab. 2 Specs. of the 3-D scanning elastic-backscatter portable lidar instrument.

## 7. CONCLUSIONS

A dual-window 3-D scanning portable backscatter lidar has been presented. In Sect. 2 the reception stage of a backscatter system has been studied as a mapping function that transforms the dynamic range of the input optical return power to that of the analog-to-digital converter (ADC). Practical measurements have shown that there are instances in which the dynamic range of the ADC is not enough to properly quantize dim far returns. These situations are not only typical of cirrus clouds and stratospheric observations, nevertheless they are the most frequent cases, but also of situations whose range of full overlap lies around 200 m or less. When simultaneous short- and far-range exploration is required, it has been shown that the dual window approach offers a more convenient solution. By means of this novel procedure, the exploration range is divided into two windows or segments so that at interspersed pulses, each of these windows is mapped into the ADC dynamic range using Eq.(1) transfer function. Implementation of the double-window technique implies a more involved electronic system design, its minimum specs. being a synchronized architecture and an optoelectronic receiver that must feature digitally controlled gain, offset and fast enable/disable. A possible architecture has been outlined in Sect.3 and Fig.3.

As a result of the dual window technique, dim far returns can be expanded to fill virtually the full range of the acquisition card. Contrary to what happened to the single window approach, for which peak returns may force a reduced gain G to avoid unwanted saturation, the dual window approach enables the far-range exploring window to usually operate at much higher gains. As discussed in Sect. 4, Eq.(7) high gain operation represents a boost in the S/N ratio.

Finally, Sect. 5 has given basic clues to calibrate the optical returns in terms of absolute power and, Sect. 6 an overview of the lidar instrument built.

## ACKNOWLEDGEMENTS

We wish to acknowledge the sponsorship of the European Union under the EARLINET (European Aerosol Research Lidar Network to Establish an Aerosol Climatology) contract UE EVR1-CT-1999-40003 and that of the CIRIT (Interdepartmental Commission for Research and Technological Innovation, Generalitat de Catalunya) under the government project IMMPACTE.

## REFERENCES

[1] L.D. Smullin and G. Fiocco, *Nature (London)* **194,** 1267 (1962); G. Fiocco and L.D. Smullin, *ibid.* **199,** 1275 (1963).

[2] R.T.H. Collis and P.B. Russell, "Lidar Measurement of Particles and Gases by Elastic Backscattering and Differential Absorption," Chap.4 in Laser Monitoring of the Atmosphere, E.D. Hinkley, Ed., (Springer-Verlag, New York, 1976), pp.71-102.

[3] C. Soriano, F. Rocadenbosch, C. Puente, A. Rodríguez, J. M. Baldasano, A. Comerón, "Confirmation of a multilayer arrangement of aerosols in the Barcelona air basin using two independent lidar systems." Proc. SPIE, European Symposium on Remote Sensing. Spectroscopic Atmospheric Environmental Monitoring Techniques (EUROPTO 98), Vol. 3493, pp. 212-222, 21-25 Sept. 1998. ISBN 0-8194-2952-X.

[4] F. Rocadenbosch, A. Comerón and D. Pineda, "Assessment of lidar inversion errors for homogeneous atmospheres," Appl. Opt. 37 (12), 2199-2206 (1998).

[5] F. Rocadenbosch, G. Vázquez, A. Comerón, "Adaptive Filter Solution For Processing Lidar Returns: Optical Parameter Estimation," Appl. Opt. 37 (30), 7019-7034 (1998).

[6] F. Rocadenbosch, C. Soriano, A. Comerón, J.Mª. Baldasano, "Lidar Inversion Of Atmospheric Backscatter And Extinction-To-Backscatter Ratios By Use Of A Kalman Filter," Appl. Opt. 38 (15), 3175-3189 (1999).

[7] F. Rocadenbosch, A. Comerón, "Error Analysis For The Lidar Backward Inversion Algorithm," Appl. Opt. 38, 4461-4474 (1999).

[8] A.B. Carlson, "Coded Pulse Modulation," Chap.12 in *Communication Systems*, 177-178, 3rd. Edition, McGRAW-HILL, Singapore, (1986).

[9] F. Rocadenbosch, A. Comerón, "Optical receiver DC-9.2MHz for non-guided optical communications and optical teledetection." Patent no. P-9700675. Spanish Office of Patents and Brands.

[10] W.B. Jones, *Introduction to Optical Fiber Communication Systems*, (Holt, Rinehart & Winston, (HRW), New York, 1988), Chaps.7,8.

[11] R.J. Barlow, "Least Squares", Chap.6 in *Statistics: A Guide To The Use Of Statistical Methods In The Physical Sciences*, F. Mandl, R.J. Ellison, D.J. Sandiford, Eds., (Wiley, Chichester, England, 1989).